Advances in Aircraft and Spacecraft Science, *Vol. 12, No. 2 (2025) 177-195*
https://doi.org/10.12989/aas.2025.12.2.177

Third-order shear deformable porous metamaterial toroidal shells with arc-type auxetic core: A stability analysis

Mohammadhossein Goudarzfallahi[1], Ali Alinia Ziazi[1] and Farzad Ebrahimi*[2]

[1]*Department of Mechanical Engineering, SR.C., Islamic Azad University, Tehran, Iran*
[2]*Department of Mechanical Engineering, Faculty of Engineering, Imam Khomeini International University, Qazvin, Iran*

(Received September 15, 2024, Revised May 3, 2025, Accepted June 25, 2025)

Abstract. This study explores the influence of porosity on the stability behavior of shear-deformable auxetic-core sandwich-structured toroidal shell segments (TSSs) with porous carbon nanotube (CNT)-reinforced face sheets supported by a Kerr-type elastic foundation and subjected to external pressure. The CNTs are embedded in a polymer matrix throughout the face sheet thickness, with three distinct porosity distribution patterns examined: uniform, symmetric, and asymmetric. The metamaterial core features an arc-type auxetic design inspired by the traditional re-entrant honeycomb structure, with curved ribs that facilitate a smooth transition between adjacent unit cells, reducing stress concentrations. The Kerr elastic foundation is modeled with three parameters: a shear layer in the middle and spring layers at the top and bottom. The governing equations for the TSSs are derived using Reddy's third-order shear deformation theory (TSDT), accounting for von Kármán-type geometric nonlinearity. A three-term deflection solution, based on simply supported boundary conditions, is employed, and the Galerkin method is used to establish the nonlinear load-deflection relationship. The validity of the approach is confirmed through a comparative analysis with existing literature, showing good agreement with theoretical results. Numerical findings provide a detailed analysis of how porosity parameters, including coefficient and distribution type, influence the stability of sandwich TSSs.

Keywords: arc-type auxetic metamaterial core; carbon nanotube-reinforced composite; Kerr-type elastic foundation; nonlinear stability; porosity; toroidal shell segment; TSDT

1. Introduction

Auxetic materials are attracting growing interest in research and applications across various industries due to their lightweight nature and exceptional ability to absorb impact impulses. Enhanced energy absorption, shear resistance, energy harvesting, and high damping capacity are among the key mechanical attributes these metamaterials have been shown to improve (Ebrahimi 2024). Numerous studies have investigated the mechanical performance of auxetic plate and shell structures. Ebrahimi and Dadashi (2023) explored the vibration behavior of composite cylindrical shells with auxetic cores under combined loading. Li and Liu (2022) studied thermal buckling and free vibration in sandwich shells featuring tunable auxetic honeycomb cores. Ebrahimi and Ahari (2024) analyzed the buckling of graphene origami-enabled auxetic metamaterial (GOEAM)

*Corresponding author, Associate Professor, E-mail: febrahimy@eng.ikiu.ac.ir

http://www.techno-press.org/?journal=aas&subpage=7 ISSN: 2287-528X (Print), 2287-5271 (Online)

nanoplates. Wang and Fu (2024) reported enhanced sound transmission loss in sandwich composite doubly curved shells with arc-type auxetic cores compared to re-entrant honeycombs. Additionally, Fu *et al.* (2024) assessed the low-velocity impact performance of sandwich shells featuring arc-type auxetic cores.

Carbon nanotubes (CNTs) are highly suitable for enhancing composite materials due to their exceptional mechanical, thermal, and electrical properties. When incorporated as fibers, they can be distributed within a polymeric matrix in either a uniform distribution (UD) or functionally graded (FG) manner (Ebrahimi and Dabbagh 2020). Shen (2011a, b) conducted a postbuckling analysis of FG-CNTRC cylindrical shells using Higher-Order Shear Deformation Theory (HSDT), incorporating von Kármán-type kinematic nonlinearity. Using Reddy's third-order shear deformation theory (TSDT), Duc *et al.* (2020) investigated the nonlinear buckling behavior of imperfect CNTRC cylindrical panels. The buckling behavior of CNTRC conical shells was analyzed by Zhao *et al.* (2024). Nam *et al.* (2019) analyzed the nonlinear stability of orthogonally reinforced CNTRC cylindrical shells. Hieu and Van Tung (2021) examined the buckling and postbuckling behavior of CNTRC cylindrical shells exposed to a uniform temperature rise. Shen and Xiang (2013) provided a postbuckling analysis of CNTRC cylindrical shells under combined mechanical and thermal loading. Van Quyen *et al.* (2021) investigated the nonlinear vibration of a CNTRC-faced cylindrical sandwich panel subjected to blast loading.

Porosity, a prevalent characteristic in manufacturing processes, can substantially diminish the mechanical performance of structures, particularly affecting properties such as stiffness, Young's modulus, and density. As a result, considerable research has recently been devoted to examining the mechanical behavior of porous materials at various scales. For instance, Ebrahimi *et al.* (2019) investigated the vibrational properties of porous metal foam cylindrical shells with different porosity distributions. Rabia *et al.* (2020) analyzed the thermo-mechanical behavior of FG plates on elastic foundations. Ebrahimi *et al.* (2021) explored the free vibration characteristics of sandwich plates made from porous electro-magneto-elastic materials. Mahesh and Ponnusami (2022) examined the nonlinear behavior of smart sandwich plates with auxetic cores. Ebrahimi and Seyfi (2022) focused on wave propagation in porous metal foam plates on Kerr substrates. Kablia *et al.* (2022) studied the dynamic behavior of imperfect FG plates with varying porosity rates. Medjdoubi *et al.* (2023) investigated shear correction factors in FG porous beams, while Ebrahimi *et al.* (2024) addressed the buckling behavior of sandwich nanoplates with magnetostrictive cores. Ebrahimi and Seyfi (2024) examined flexural wave propagation in porous metal foam beams with different porosity distributions. Zohra *et al.* (2024) assessed the impact of porosity on the buckling behavior of FG plates under thermal conditions. Ellali *et al.* (2024) explored thermal buckling in porous FG rectangular plates with piezoelectric actuators. Li and Li (2024) examined how microstructure influences the macroscopic properties of metamaterials, mainly focusing on the size-dependent surface effect, where surface elasticity becomes more significant as the microstructure's size approaches the thickness of the structure. Ebrahimi and Dabbagh (2023) studied the effects of porosity on CNTRC meta-composite structures. Toroidal shell segments (TSSs) are widely used in aeronautical, underwater, and civil engineering applications due to their adaptable curvature, which enables diverse structural configurations. Their static and dynamic stability has been the subject of extensive research. Stein and McElman (1965) employed classical shell theory (CST) to examine the buckling of TSSs under external pressure. Using Donnell's shell theory, Oyesanya (2005) analyzed the stability of imperfect TSSs subjected to external pressure. Building on CST and the approximation by Stein and McElman (1965), Phuong *et al.* (2021) studied the nonlinear buckling and postbuckling behavior of FG-GRC TSSs under radial pressure

in a thermal environment.

More recently, several studies—building on Stein and McElman's (1965) approximation and CST—have focused on improving the buckling and postbuckling performance of TSSs through the integration of advanced nanocomposites and auxetic cores. Van Tien *et al.* (2022) conducted a nonlinear analysis of sandwich TSSs with a honeycomb auxetic core and CNT-reinforced face sheets under radial pressure, employing the Galerkin method to derive their buckling and postbuckling responses. Ebrahimi *et al.* (2024a) assessed the stability of TSSs with a GOREAM core and CNTRC face sheets, revealing improved performance compared to conventional re-entrant auxetic metamaterials. In a subsequent study, Ebrahimi *et al.* (2024b) examined the same composite TSSs under combined mechanical loads. Dung and Vuong (2017) applied TSDT to investigate the buckling and postbuckling behavior of FGM TSSs under uniform radial pressure. Ebrahimi *et al.* (2024c) studied the stability of porous GOREAM core TSSs. Furthermore, based on TSDT, Ebrahimi *et al.* (2024d) analyzed TSSs with arc-type auxetic cores. More recently, Ebrahimi *et al.* (2025a) investigated GOREAM core TSSs under axial compression, while Ebrahimi *et al.* (2025b) explored the stability response of TSSs incorporating a bio-inspired auxetic core. Hieu and Van Tung (2020a, b) used first-order shear deformation theory (FSDT) to conduct an analytical study on the buckling of CNTRC TSSs surrounded by elastic media under various loading conditions. Similarly, Vuong and Duc (2019, 2020a, b) investigated the buckling and postbuckling behavior of FG TSSs using TSDT.

To the authors' knowledge, no prior studies based on HSDT have examined the stability behavior of shear-deformable sandwich TSSs with auxetic cores under external pressure. Existing works have predominantly focused on thin shells while neglecting shear deformation, which is essential for accurately capturing postbuckling responses. Moreover, the influence of porosity—a typical result of advanced manufacturing—on the stability of such structures has been largely overlooked, particularly for sandwich TSSs with auxetic cores. The originality and novelty of this study lie in addressing these gaps by incorporating the effects of both shear deformation and porosity into the analysis of sandwich TSSs. Accordingly, this research investigates the nonlinear stability of shear-deformable sandwich TSSs with porous CNT-reinforced face sheets and an arc-type auxetic core supported by a Kerr elastic foundation and subjected to external pressure. The outcomes provide deeper insights into the structural behavior of such advanced composites, supporting more accurate and stable design strategies.

2. Geometric configuration and material characterization

2.1 Geometric configuration

TSSs with concave and convex configurations are considered, as depicted in Fig. 1, where a and R denote the longitudinal and circumferential radii, L indicates the longitudinal length of the shell, and h is the TSS's total thickness. A coordinate system (x, y, z) is defined as having the origin O located at the mid-surface and edge of the shell (Fig. 1). The x and y axes represent the longitudinal and circumferential directions, with the z-axis aligning in the radial direction and pointing inward. The sandwich-structured composite structure comprises an auxetic core with a thickness of h_2 and two face sheets reinforced with CNTs, each having a thickness of h_1 (see Fig. 2). The sandwich TSSs are surrounded by Kerr's foundation, comprising two springs linked by a shear layer.

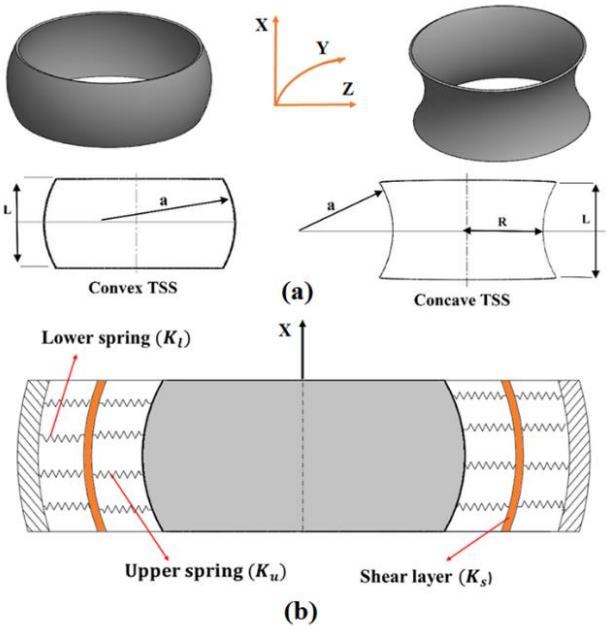

Fig. 1 Schematic of TSSs supported by a Kerr-type elastic foundation

2.2 Material characterization

2.2.1 Arc-type auxetic core

The core layer of the sandwich TSS consists of an arc-type auxetic structure (see Fig. 2). The elastic moduli of the arc-type auxetic metamaterial core can be represented as (Ebrahimi *et al.* 2024d)

$$E_1^c = \frac{a_1 \cdot E_c \cdot d_1^3}{12 b_1 r_c^3 (4\theta\cos^2\theta - 3\sin 2\theta + 2\theta)}$$
$$E_2^c = \frac{b_1 \cdot E_c \cdot d_1^3}{3 a_1 r_c^3 [4\theta\sin^2\theta + 3\sin 2\theta + 2\theta - 8\sin\theta]}$$
$$\nu_{12}^c = \frac{a_1 (3\cos 2\theta/4 + \theta\sin 2\theta/2 - \cos\theta + 1/4)}{b_1 (2\theta\cos^2\theta - 3\sin 2\theta/2 + \theta)} \quad (1)$$
$$\nu_{21}^c = \frac{-4\, a_1 (\sin^2\theta + 2\cos\theta(1-\cos\theta) - \theta\sin 2\theta)}{a_1 (2\theta + 3\sin 2\theta + 4\theta\sin^2\theta - 8\sin\theta)}$$
$$G_{13}^c = G_{23}^c = \frac{E_c \cdot d_1^3}{8 r_c^3 [\theta\sin^2(\theta) + 2\sin(\theta)(\cos(\theta) - 1) + \theta/2 - \sin(2\theta)/4]}$$

where E_c represents the Young's modulus of the original material. Furthermore, the key geometric parameters a_1 and b_1 are expressed as

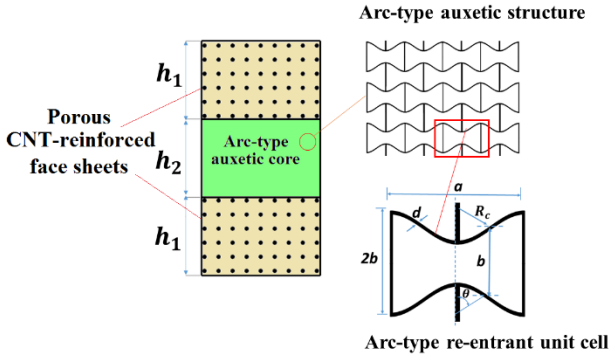

Fig. 2 Schematic of sandwich composite with arc-type auxetic core and porous CNT-reinforced face sheets

$$\begin{gathered} a_1 = 2(2r_c + d_1) \times \sin\theta, \\ b_1 = 2(2r_c + d_1) \times \cos\theta \\ S_1 = 80\pi(2r_c d_1 + d_1^3)/360^{\circ} + 4d_1 r_c \\ S_2 = 2a_1 b_1 \end{gathered} \tag{2}$$

2.2.2 Porous CNT-reinforced face sheets

The sandwich structure's face sheets are CNT-reinforced with UD and FG through-thickness distributions (Fig. 2), embedded in a polymer matrix, and aligned longitudinally or circumferentially. The CNT volume fractions are defined as Shen (2011a, b)

$$\begin{gathered} V_{CNT} = \bar{V}_{CNT} \ (\text{UD}) \\ V_{CNT} = \left(\frac{4|z|}{h_1}\right)\bar{V}_{CNT} \ (\text{FG}-\text{X}) \end{gathered} \tag{3}$$

The elastic properties of the orthotropic CNT-reinforced face sheets are evaluated using the extended rule of mixtures, as proposed by Shen (2011a, b).

$$\begin{gathered} E_{11}^{CNTRC} = V_{ma}E_{ma} + \eta_1 V_{CNT}E_{11}^{CNT},\ E_{22}^{CNTRC} = \eta_2 / \left(\frac{V_{CNT}}{E_{22}^{CNT}} + \frac{V_{ma}}{E_{ma}}\right) \\ G_{12}^{CNTRC} = \eta_3 / \left(\frac{V_{CNT}}{G_{12}^{CNT}} + \frac{V_{ma}}{G_{ma}}\right),\ \nu_{12}^{CNTRC} = V_{ma}\nu_{ma} + V_{CNT}\nu_{12}^{CNT} \end{gathered} \tag{4}$$

in which E_{11}^{CNT}, E_{22}^{CNT}, and G_{12}^{CNT} represent the elastic moduli for the CNTs, while E_{ma} and G_{ma}denote the elastic moduli of the matrix material. Additionally, η_j(j=1, 2, 3) represents the efficiency parameter for the CNTs, and V_{CNT} and V_{ma} are the volume fractions of the CNTs and the matrix, which satisfy $V_{\mathrm{CNT}} + V_{ma} = 1$.

Furthermore, Poisson's ratios for the CNTs and matrix materials are referred to as ν_{12}^{CNT} and ν_{ma}, respectively.

This study proposes three types of porosity for the CNT-reinforced face sheets. Those patterns include face sheets with void distributions in uniform, symmetric, and asymmetric patterns. In the subsequent formulations, e_0 and e_m represent the porosity and density coefficients.

For uniform porosity distribution, the effective properties can be expressed as (Ebrahimi *et al.* 2019, Ebrahimi and Seyfi 2022).

$$\begin{aligned} E(z) &= E_1(1-e_0\lambda) \\ G(z) &= G_1(1-e_0\lambda) \\ \rho(z) &= \rho_1\sqrt{1-e_0\lambda} \end{aligned} \tag{5}$$

Moreover, the effective properties of symmetrically porous face sheets can be estimated as follows (Ebrahimi *et al.* 2019, Ebrahimi and Seyfi 2022)

$$\begin{aligned} E(z) &= E_1\left(1-e_0 cos\left(\frac{\pi z}{h}\right)\right) \\ G(z) &= G_1\left(1-e_0 cos\left(\frac{\pi z}{h}\right)\right) \\ \rho(z) &= \rho_1\left(1-e_m cos\left(\frac{\pi z}{h}\right)\right) \end{aligned} \tag{6}$$

The effective properties describing the asymmetric porosity distribution pattern are represented as (Ebrahimi *et al.* 2019, Ebrahimi and Seyfi 2022)

$$\begin{aligned} E(z) &= E_1\left(1-e_0 cos\left(\frac{\pi z}{2h}+\frac{\pi}{4}\right)\right) \\ G(z) &= G_1\left(1-e_0 cos\left(\frac{\pi z}{2h}+\frac{\pi}{4}\right)\right) \\ \rho(z) &= \rho_1\left(1-e_m cos\left(\frac{\pi z}{2h}+\frac{\pi}{4}\right)\right) \end{aligned} \tag{7}$$

where E_1, G_1, and ρ_1 represent the maximum Young's modulus, shear modulus, and mass density of the porous face sheets, while E_2, G_2, and ρ_2 denote their minimum values. Additionally, e_0 and e_m, which are the porosity and density coefficients, are derived from these extremum values as follows (Ebrahimi *et al.* 2019, Ebrahimi and Seyfi 2022)

$$\begin{aligned} e_0 = 1-\frac{E_2}{E_1} = 1-\frac{G_2}{G_1}, \quad (0<e_0<1) \\ e_m = 1-\frac{\rho_2}{\rho_1} \end{aligned} \tag{8}$$

In this approach, the Poisson's ratio is considered constant because of negligible variations. The term λ in Eqs. (1) -(3) can be calculated as (Ebrahimi *et al.* 2019, Ebrahimi and Seyfi 2022)

$$\lambda = \frac{1}{e_0}-\frac{1}{e_0}\left[\frac{2}{\pi}\sqrt{1-e_0}-\frac{2}{\pi}+1\right]^2 \tag{9}$$

3. Governing equations

This study employs the TSDT, developed by Reddy and Liu (1987), and incorporates von Kármán nonlinearity to derive the nonlinear governing equations for analyzing the nonlinear stability characteristics of porous sandwich TSSs under uniform external pressure and supported by a Kerr elastic foundation.

Based on the TSDT, the displacement components at a distance z from the mid-surface are expressed as (Reddy and Liu 1987, Reddy 2003)

$$\begin{pmatrix}\bar{u}\\ \bar{v}\\ \bar{w}\end{pmatrix}=\begin{pmatrix}u+z\phi_x-\frac{4}{3h^2}z^3(\phi_x+\frac{\partial w_0}{\partial x})\\ v+z\phi_y-\frac{4}{3h^2}z^3(\phi_y+\frac{\partial w_0}{\partial y})\\ w\end{pmatrix} \tag{10}$$

Here, u, v, and w represent the mid-surface displacement components.

The strain components, incorporating von Kármán nonlinear terms, are given by (Reddy and Liu 1987, Reddy 2003)

$$\begin{pmatrix}\varepsilon_x\\ \varepsilon_y\\ \gamma_{xy}\end{pmatrix}=\begin{pmatrix}\varepsilon_x^0\\ \varepsilon_y^0\\ \gamma_{xy}^0\end{pmatrix}+z\begin{pmatrix}k_x^{(1)}\\ k_y^{(1)}\\ k_{xy}^{(1)}\end{pmatrix}+z^3\begin{pmatrix}k_x^{(3)}\\ k_y^{(3)}\\ k_{xy}^{(3)}\end{pmatrix}$$
$$\begin{pmatrix}\gamma_{xz}\\ \gamma_{yz}\end{pmatrix}=\begin{pmatrix}\gamma_{xz}^0\\ \gamma_{yz}^0\end{pmatrix}+z^2\begin{pmatrix}k_{xz}^{(2)}\\ k_{yz}^{(2)}\end{pmatrix} \tag{11}$$

The strain components at the mid-surface of the shell are expressed as (Stein and McElman 1965, Reddy 2003)

$$\begin{pmatrix}\varepsilon_x^0\\ \varepsilon_y^0\\ \gamma_{xy}^0\end{pmatrix}=\begin{pmatrix}u_{,x}-w/a+w_{,x}^2/2\\ v_{,y}-w/R+w_{,y}^2/2\\ u_{,y}+v_{,x}+w_{,x}w_{,y}\end{pmatrix}$$
$$\begin{pmatrix}\gamma_{xz}^0\\ \gamma_{yz}^0\end{pmatrix}=\begin{pmatrix}\phi_x+w_{,x}\\ \phi_y+w_{,y}\end{pmatrix} \tag{12}$$

Furthermore

$$\begin{pmatrix}k_x^{(1)}\\ k_y^{(1)}\\ k_{xy}^{(1)}\end{pmatrix}=\begin{pmatrix}\phi_{x,x}\\ \phi_{y,y}\\ \phi_{x,y}+\phi_{y,x}\end{pmatrix}$$
$$\begin{pmatrix}k_x^{(3)}\\ k_y^{(3)}\\ k_{xy}^{(3)}\end{pmatrix}=-c\begin{pmatrix}\phi_{x,x}+w_{,xx}\\ \phi_{y,y}+w_{,yy}\\ \phi_{x,y}+\phi_{y,x}+2w_{,xy}\end{pmatrix} \tag{13}$$
$$\begin{pmatrix}k_{xz}^{(2)}\\ k_{yz}^{(2)}\end{pmatrix}=-3c\begin{pmatrix}\phi_x+w_{,x}\\ \phi_y+w_{,y}\end{pmatrix}\quad c=4/3h^2$$

Applying Hooke's law to the porous sandwich shells yields

$$\begin{pmatrix}\sigma_x\\ \sigma_y\\ \sigma_{yz}\\ \sigma_{xz}\\ \sigma_{xy}\end{pmatrix}=\begin{bmatrix}Q_{11}&Q_{12}&0&0&0\\ Q_{12}&Q_{22}&0&0&0\\ 0&0&Q_{55}&0&0\\ 0&0&0&Q_{44}&0\\ 0&0&0&0&Q_{66}\end{bmatrix}\begin{Bmatrix}\varepsilon_x\\ \varepsilon_y\\ \gamma_{yz}\\ \gamma_{xz}\\ \gamma_{xy}\end{Bmatrix} \tag{14}$$

where

$$Q_{11}=\frac{E_{11}}{1-v_{12}v_{21}},Q_{12}=\frac{v_{21}E_{11}}{1-v_{12}v_{21}},Q_{22}=\frac{E_{22}}{1-v_{12}v_{21}}$$
$$Q_{44}=G_{23},\quad Q_{55}=G_{13},\quad Q_{66}=G_{12} \tag{15}$$

The force and moment resultants are represented as

$$(N_i,M_i,P_i)=\int_{-h/2}^{h/2}\sigma_i\,(1,z,z^3)dz,\quad i=x,y,xy$$
$$(Q_j,R_j)=\int_{-h/2}^{h/2}\sigma_{iz}\,(1,z^2)dz,\quad i=x,y \tag{16}$$

Substituting Eq. (11) into Eq. (14), followed by incorporating the results into Eq. (16), provides the constitutive relations as

$$\begin{gathered}
N_x=A_{11}\epsilon_x^0+A_{12}\epsilon_y^0+A_{13}k_x+A_{14}k_y+A_{15}k_x^3+A_{16}k_y^3-A_{17}\Phi_{,y}\\
N_y=A_{12}\epsilon_x^0+A_{22}\epsilon_y^0+A_{23}k_x+A_{24}k_y+A_{25}k_x^3+A_{26}k_y^3-A_{27}\Phi_{,y}\\
N_{xy}=A_{31}\gamma_{xy}^0+A_{32}k_{xy}+A_{33}k_{xy}^3\\
M_x=A_{13}\epsilon_x^0+A_{14}\epsilon_y^0+A_{43}k_x+A_{44}k_y+A_{45}k_x^3+A_{46}k_y^3-A_{17}\Phi_{,y}\\
M_y=A_{14}\epsilon_x^0+A_{24}\epsilon_y^0+A_{44}k_x+A_{54}k_y+A_{46}k_x^3+A_{56}k_y^3-A_{27}\Phi_{,y}\\
M_{xy}=A_{32}\gamma_{xy}^0+A_{62}k_{xy}+A_{63}k_{xy}^3\\
P_x=A_{71}\epsilon_x^0+A_{16}\epsilon_y^0+B_{73}k_x+A_{46}k_y+A_{75}k_x^3+A_{76}k_y^3-A_{17}\Phi_{,x}\\
P_y=A_{16}\epsilon_x^0+A_{82}\epsilon_y^0+A_{46}k_x+A_{84}k_y+A_{76}k_x^3+A_{86}k_y^3-A_{27}\Phi_{,y}\\
P_{xy}=A_{33}\gamma_{xy}^0+A_{63}k_{xy}+A_{93}k_{xy}^3Q_x=A_{94}\gamma_{xy}^0+A_{95}k_{xz}^2\\
Q_y=A_{96}\gamma_{xy}^0+A_{97}k_{yz}^2\\
K_x=A_{98}\gamma_{xz}^0+A_{99}k_{xz}^2\\
K_y=A_{100}\gamma_{xy}^0+A_{101}k_{yz}^2
\end{gathered} \tag{17}$$

Here, the coefficients A_{ij} are determined, as explained by Duc *et al.* (2020). Based on TSDT, the nonlinear equilibrium equations for porous sandwich TSSs surrounded by a Kerr elastic foundation are given as follows (Reddy 2003)

$$\begin{pmatrix}\bar{u}\\ \bar{v}\\ \bar{w}\end{pmatrix}=\begin{pmatrix}u+z\phi_x-\frac{4}{3h^2}z^3(\phi_x+\frac{\partial w_0}{\partial x})\\ v+z\phi_y-\frac{4}{3h^2}z^3(\phi_y+\frac{\partial w_0}{\partial y})\\ w\end{pmatrix} \tag{18}$$

$$\begin{gathered}N_{x,x}+N_{xy,y}=0\\ N_{xy,x}+N_{y,y}=0\end{gathered} \tag{19}$$

$$\begin{gathered}Q_{x,x}+Q_{y,y}-3c(R_{x,x}+R_{y,y})+c(P_{x,xx}+2P_{xy,xy}+P_{y,yy})+\frac{N_x}{a}+\frac{N_y}{R}+p_0+N_xw_{xx}\\+2N_{xy}w_{xy}+N_yw_{yy}-k_1w+k_2(w_{xx}+w_{yy})=0\end{gathered} \tag{20}$$

$$M_{x,x} + M_{xy,y} - Q_x + 3cR_x - c\left(P_{x,x} + P_{xy,y}\right) = 0 \tag{21}$$

$$M_{y,y} + M_{xy,x} - Q_y + 3cR_y - c\left(P_{y,y} + P_{xy,x}\right) = 0 \tag{22}$$

Here, the symbol p_0 represents the uniform external pressure. Additionally, K_1 and K_2 denote the elastic foundation parameters described by Ebrahimi *et al.* (2024d). Next, the Airy stress function $\varsigma(x, y)$ is introduced as (Ebrahimi *et al.* 2024d)

$$\varsigma_{,yy} = N_x,\ \ \varsigma_{,xx} = N_y,\ \ \varsigma_{,xy} = -N_{xy} \tag{23}$$

Accordingly, from Eq. (17), the strain components can be obtained as

$$\begin{aligned}
\epsilon_x^0 &= \frac{A_{22}}{\Delta}\varsigma_{,yy} - \frac{A_{12}}{\Delta}\varsigma_{,xx} - \frac{A_{13}A_{22} - A_{14}A_{12}}{\Delta}k_x^1 - \frac{A_{14}A_{22} - A_{24}A_{12}}{\Delta}k_y^1 \\
&\quad - \frac{A_{15}A_{22} - A_{16}A_{12}}{\Delta}k_x^3 - \frac{A_{16}A_{22} - A_{26}A_{12}}{\Delta}k_y^3 \\
\epsilon_y^0 &= \frac{A_{11}}{\Delta}\varsigma_{,xx} - \frac{A_{12}}{\Delta}\varsigma_{,yy} - \frac{A_{11}A_{14} - A_{13}A_{12}}{\Delta}k_x^1 - \frac{A_{11}A_{24} - A_{14}A_{12}}{\Delta}k_y^1 \\
&\quad - \frac{A_{11}A_{16} - A_{15}A_{12}}{\Delta}k_x^3 - \frac{A_{11}A_{26} - A_{16}A_{12}}{\Delta}k_y^3 \\
\gamma_{xy}^0 &= -\frac{1}{A_{31}}\varsigma_{,xy} - \frac{A_{32}}{A_{31}}k_{xy}^1 - \frac{A_{33}}{A_{31}}k_{xy}^3
\end{aligned} \tag{24}$$

In which $\Delta = A_{11}A_{22} - A_{12}^2$.

From Eq. (12), the compatibility equation for porous sandwich-structured TSSs is written as

$$\varepsilon_{x,yy}^0 + \varepsilon_{y,xx}^0 - \gamma_{xy,xy}^0 + \frac{1}{R}w_{,xx} + \frac{1}{a}w_{,yy} - w_{,xy}^2 + w_{,xx}w_{,yy} = 0 \tag{25}$$

Upon substituting Eq. (24) into Eq. (17) and applying the resulting expressions in Eqs. (19)-(22), the equilibrium equations are expressed as follows

$$H_{11}(\phi_x) + H_{12}(\phi_y) + H_{13}(w) + H_{14}(\varsigma) + P(w, \varsigma) + p_0 = 0 \tag{26}$$

$$H_{21}(\phi_x) + H_{22}(\phi_y) + H_{23}(w) + L_{24}(\varsigma) = 0 \tag{27}$$

$$H_{31}(\phi_x) + H_{32}(\phi_y) + H_{33}(w) + L_{34}(\varsigma) = 0 \tag{28}$$

where

$$\begin{gathered}
H_{11}(\varphi_x) = D_{11}\varphi_{x,x} + D_{12}\varphi_{x,xxx} + D_{13}\varphi_{y,xyy}\,, H_{12}\left(\varphi_y\right) \\
= D_{21}\varphi_{y,y} + D_{22}\varphi_{y,xxy} + D_{23}\varphi_{y,yyy} \\
H_{13}(w) = D_{31}w_{,xx} + D_{32}w_{,yy} + D_{33}w_{,xxxx} + D_{34}w_{,yyyy} + D_{35}w_{,xxyy} - k_1 w + \\
k_2\left(w_{,xx} + w_{,yy}\right) \\
H_{14}(\varsigma) = D_{11}^*\varsigma_{,xxxx} + D_{12}^*\varsigma_{,xxyy} + D_{13}^*\varsigma_{,yyyy} + \frac{\varsigma_{,xx}}{R} + \frac{\varsigma_{,yy}}{a}\,, H_{22}\left(\varphi_y\right) = D_{51}\varphi_{y,xy} \\
P(w, \varsigma) = \varsigma_{,yy}w_{,xx} - 2\varsigma_{,xy}w_{,xy} + \varsigma_{,yy}w_{,yy}\,, H_{21}(\varphi_x) = D_{41}\varphi_x + D_{42}\varphi_{x,xx} + D_{43}\varphi_{x,yy} \\
H_{23}(w) = D_{61}w_{,x} + D_{62}w_{,xxx} + D_{63}w_{,xyy}\,, H_{24}(\varsigma) = D_{21}^*\varsigma_{,xyy} + D_{22}^*\varsigma_{,xxx} \\
H_{31}(\varphi_x) = D_{71}\varphi_{x,xy}\,, H_{32}\left(\varphi_y\right) = D_{81}\varphi_{y,yy} + D_{82}\varphi_{y,xx} + D_{83}\varphi_y \\
H_{33}(w) = D_{91}w_{,y} + D_{92}w_{,xxy} + D_{93}w_{,yyy}\,, H_{34}(\varsigma) = D_{31}^*\varsigma_{,yyy} + D_{32}^*\varsigma_{,yxx}
\end{gathered} \tag{29}$$

The expressions for D_{ij} and D_{ij}^{*} are obtained as described by Ebrahimi *et al.* (2024d). By inserting Eq. (24) into Eq. (25), we obtain the compatibility equation for the porous sandwich TSSs as

$$I_1\varsigma_{,yyyy} + I_2\varsigma_{,xxxx} + I_3\varsigma_{,xxyy} + I_4\varsigma_{y,yyy} + I_5\phi_{x,xyy} + I_6\varphi_{x,xxx} + I_7\varphi_{y,xxy} + I_8 w_{,xxxx} + I_9 w_{,yyyy} + I_{10} w_{,xxyy} = w_{,xy}^2 - w_{,xx}w_{,yy} - \frac{w_{,xx}}{R} - \frac{w_{,yy}}{a} \tag{30}$$

where the variables I_j $(j = 1,2,\ldots,10)$ were presented by Ebrahimi *et al.* (2024d).

Eqs. (26)-(28) and Eq. (30) serve as the governing equations for analyzing the stability characteristics of porous sandwich shells.

4. Analytical solution

This study considers the porous sandwich TSSs to be simply supported at the two butt-ends, freely movable, and subjected to an external uniform pressure p_0. The boundary conditions are defined as (Ebrahimi *et al.* 2024d)

$$w = 0, M_x = 0, N_x = 0, N_{xy} = 0, \phi_y = 0 \quad \text{at} \quad x = 0; x = L \tag{31}$$

The deflection solution that satisfies the boundary conditions is assumed to be (Ebrahimi *et al.* 2024d)

$$w = W_0 + W_1 sin\frac{m\pi x}{L} sin\frac{ny}{R} + W_2 sin^2\frac{m\pi x}{L} \tag{32}$$

Where *m* and *n* are the half-wave numbers in the *x* and *y* directions, respectively. The first term denotes the pre-buckling deflection amplitude, while the second and third terms correspond to the linear and nonlinear buckling shapes, respectively.

Considering the boundary conditions provided in Eq. (31) and substituting Eq. (32) into equation (Eq. (29)), the stress function $\varsigma(x,y)$ is obtained as follows:(Ebrahimi *et al.* 2024d)

$$\varsigma = \varsigma_1\cos(\tfrac{2m\pi x}{L}) + \varsigma_2\cos(\tfrac{2ny}{R}) + \varsigma_3\sin(\tfrac{3m\pi x}{L})\sin(\tfrac{ny}{R}) + \varsigma_4\sin(\tfrac{3m\pi x}{L})\sin(\tfrac{ny}{R}) - \tfrac{1}{2}\sigma_{0y}hx^2 \tag{33}$$

where σ_{0y} denotes the negative average circumferential stress. On the other hand, the obtained solution for the stress function should satisfy both Eq. (27) and Eq. (28). This requirement can be fulfilled if the functions ϕ_x and ϕ_y are expressed as

$$\begin{aligned}\phi_x(x,y) &= C_1\cos\left(\frac{m\pi x}{L}\right)\sin\left(\frac{ny}{R}\right) + C_2\sin\left(\frac{2m\pi x}{L}\right) + C_3\cos\left(\frac{3m\pi x}{L}\right)\sin\left(\frac{ny}{R}\right)\\ \phi_y(x,y) &= C_4\cos\left(\frac{ny}{R}\right)\sin\left(\frac{m\pi x}{L}\right) + C_5\cos\left(\frac{ny}{R}\right)\sin\left(\frac{3m\pi x}{L}\right) + C_6\sin\left(\frac{2ny}{R}\right)\end{aligned} \tag{34}$$

Consequently, upon substituting Eqs. (34)-(35) into Eqs. (27)-(28) and solving the resulting equations, the parameters $\varsigma_i(i = 1,4)$ and $C_i(i = 1,6)$ can be found as

$$\varsigma_1 = -a_{15}W_2 + a_{16}W_1^2,\ \varsigma_2 = a_{12}W_1^2,\ \varsigma_3 = -\frac{d_{26}W_1 + (d_{15}d_{18}d_{22} - d_{15}d_{16}d_{20})W_1W_2}{d_{24}},$$

$$\varsigma_4 = b_{23}W_1W_2,\ C_1 = -\frac{d_{25}W_1 + (d_{15}d_{17}d_{20} + d_{15}d_{18}d_{21})W_1W_2}{d_{24}},$$

$$C_2 = a_{13}W_2 - a_{14}W_1^2,\ C_3 = b_{21}W_1W_2,\ C_4 = -\frac{d_{27}W_1+(d_{15}d_{16}d_{21}+d_{15}d_{17}d_{22})W_1W_2}{d_{24}},$$
$$C_5 = b_{22}W_1W_2,\ C_6 = a_{11}W_1^2 \tag{35}$$

Next, by Substituting Eqs. (34)-(35) into Eqs. (26)-(28) and applying the Galerkin method yields a system of algebraic equations for analyzing the stability of porous sandwich shells. This weighted residual approach enforces residual orthogonality to chosen weight functions, and integration by parts transforms the equations into weak form, enabling efficient, accurate, and convergent numerical solutions.

$$q - K_1\left(W_0 + \frac{W_2}{2}\right) - \frac{h}{R}\sigma_{0y} = 0 \tag{36}$$

$$l_{11} + l_{12}W_1^2 + l_{13}W_2 + l_{14}W_2^2 + hL^2n^2\sigma_{0y} = 0 \tag{37}$$

$$K_1W_0 + l_{16}W_1^2 + l_{17}W_2 + l_{18}W_1^2W_2 + \frac{h}{R}\sigma_{0y} = P_0 \tag{38}$$

where the coefficients l_{ij} are obtained as explained by Ebrahimi *et al.* (2024d); furthermore, the circumferential closure condition must be satisfied by the TSSs, as expressed by (Ebrahimi *et al.* 2024d)

$$\int_0^{2\pi R}\int_0^L v_{,y}dxdy = \int_0^{2\pi R}\int_0^L \left(\varepsilon_y^0 + \frac{w}{R} - \frac{1}{2}w_{,y}^2\right)dxdy = 0 \tag{39}$$

Using Eq. (24), Eq. (32), Eq. (33), and Eq. (34), this integral leads to

$$\frac{(2W_0 + W_2)}{R} - \left(\frac{n}{2R}\right)^2 W_1^2 - 2hI_2\sigma_{0y} = 0 \tag{40}$$

Inserting the average circumferential stress σ_{0y} from Eq. (36) into Eqs. (37)-(38), along with the circumferential closure condition of the shell, allows Eqs. (36)-(38) to be rewritten as

$$W_0 = S_{17}W_1^2 - W_2/2 + S_{18}P_0 \tag{41}$$

$$S_{11} + S_{12}W_0 - S_{13}W_1^2 + l_{14}W_2 - S_{15}W_2^2 - S_{16}p_0 = 0 \tag{42}$$

$$W_1^2 = \frac{S_{22}W_2}{S_{21} - S_{23}W_2} \tag{43}$$

Here, the expressions for S_{ij} are derived as outlined by Ebrahimi *et al.* (2024d) and Dung and Vuong (2017).

$$P_0 = \left\{\frac{S_{11}S_{22}}{-S_{22}+S_{23}W_2} + \frac{-S_{13}S_{21}-S_{12}S_{17}S_{21}+S_{14}S_{22}+S_{12}S_{18}S_{22}-S_{11}S_{23}}{-S_{22}+S_{23}W_2}W_2 + \right.$$
$$\left.\frac{-S_{15}S_{22}-S_{14}S_{23}-S_{12}S_{18}S_{23}}{-S_{22}+S_{23}W_2}W_2^2 + \frac{S_{15}S_{23}}{-S_{22}+S_{23}W_2}W_2^3\right\} \times \left(\frac{1}{(S_{16}-S_{12}S_{19}}\right) \tag{44}$$

By setting $W_2 = 0$ in Eq. (44), the linear upper buckling load is obtained as

$$p_0^{\text{upper}} = \frac{-S_{11}}{S_{16} - S_{12}S_{19}} \tag{45}$$

The critical buckling load for external pressure p_0^{cr} is determined by minimizing p_0^{upper} from Eq.

Table 1 Critical buckling loads p_0^{cr} (in KPa) of CNTRC cylindrical shells subjected to radial pressure ($e_0 = 0$, T=300 K, R/h=100, h=1 mm, $h_2 = 0$, $K_1 = K_2 = 0$)

L^2/Rh	V_{CNT}	Shen (2011b)		Present	
		UD	FG-X	UD	FG-X
100	0.12	42.68 (1,10)*	49.48 (1,10)	42.5919 (1,10)	48.3354 (1,10)
	0.17	70.06 (1,10)	82.76 (1,10)	69.9348 (1,10)	81.0263 (1,10)
	0.28	84.34 (1,10)	109.42 (1,10)	84.1303 (1,10)	107.931 (1,10)
300	0.12	23.40 (1,8)	25.60 (1,8)	23.3988 (1,8)	25.3212 (1,8)
	0.17	38.98 (1,8)	43.83 (1,8)	38.9749 (1,8)	43.4094 (1,8)
	0.28	45.11 (1,8)	55.84 (1,8)	45.1177 (1,8)	55.9355 (1,8)

*The numbers in brackets represent the buckling modes (m, n).

Table 2 Critical buckling loads p_0^{cr} (in MPa) of CNTRC TSSs subjected to radial pressure ($e_0 = 0$, T=300 K, R/h=80, h=1 mm, $h_2 = 2$ mm, $K_1 = 10^7$, $K_2 = 10^5$)

Shell type	V_{CNT}	Van Tien *et al.* (2022)		Present (TSDT)	
		UD	FG-X	UD	FG-X
Convex TSS	0.12	1.008 (1;5)	1.080 (1;5)	0.996405 (1,5)	1.0641 (1,5)
	0.17	1.219 (1;5)	1.325 (1;5)	1.19701 (1,5)	1.29569 (1,5)
Concave TSS	0.12	0.825 (1;4)	0.871 (1;4)	0.820598 (1,4)	0.864437 (1,4)
	0.17	0.926 (1;4)	0.993 (1;4)	0.917225 (1,4)	0.980805 (1,4)

(45) concerning m and n. From Eq. (32), the maximum deflection of the shells is given by

$$W_{\max} = W_0 + W_1 + W_2 \tag{46}$$

Inserting Eq. (41) and Eq. (43) into Eq. (46) yields the maximum deflection with respect to W_2.

$$W_{\max} = S_{17}W_1^2 + W_2/2 + S_{18}P_0 + \left(\frac{S_{22}W_2}{S_{21} - S_{23}W_2}\right)^{1/2} \tag{47}$$

Combining Eq. (44) and Eq. (47), one can obtain the postbuckling curve $P_0 - W_{max}/h$ of sandwich composite TSSs with an arch-type auxetic core and porous CNTRC face sheets.

5. Results and discussion

5.1 Validity verification

To validate the proposed method, comparative studies are performed for two specific cases involving shell geometry and material properties to confirm its accuracy.

Example 1. The first comparison involves performing a comparative study against the critical buckling loads of an unstiffened CNTRC cylindrical shell ($a\to\infty$) with no porosity under external pressure, as Shen (2011b) analyzed using HSDT. As shown in Table 1, the validation cases demonstrate satisfactory agreement between the two studies.

Example 2. The proposed approach is further validated through comparison with the results of Van Tien *et al.* (2022) for an FG-CNTRC TSS with a PMMA solid core, reinforced face sheets

Table 3 Critical buckling load results for convex TSSs based on CST and TSDT approacheswith arc-type auxetic-core and CNTRC face sheets, subjected to uniform external pressure, across various R/h ratios ($e_0 = 0, a = 4R, L = 1.5R, h_1 = 0.001$ mm, $\bar{V}_{CNT} = 0.17, K_1 = K_2 = 0$)

R/h	TSDT		CST		Difference (%)	
	UD	FG-X	UD	FG-X	UD	FG-X
10	140.538 (1,3)	158.686 (1,3)	144.942 (1,3)	164.315 (1,3)	3.13	3.55
20	33.6545 (1,4)	36.0835 (1,3)	33.8147 (1,3)	36.2668 (1,3)	0.48	0.51
50	4.9076 (1,5)	5.33432 (1,5)	4.92158 (1,5)	5.35182 (1,5)	0.28	0.33
100	1.26582 (1,7)	1.3706 (1,7)	1.26758 (1,7)	1.37281 (1,7)	0.14	0.16
200	0.307379 (2,10)	0.334214 (2,10)	0.307599 (2,10)	0.334489 (2,10)	0.07	0.08

supported by an elastic foundation, and subjected to radial pressure. As shown in Table 2, the critical buckling loads determined here are in good agreement with those predicted by Van Tien *et al.* (2022), demonstrating the accuracy and reliability of the proposed approach

5.2 *Importance of TSDT in evaluating buckling loads of thicker TSSs*

In this section, to highlight the importance of TSDT, a comparative study is conducted on the critical buckling loads of auxetic-core sandwich composite TSSs with CNTRC face sheets (assuming $e_0 = 0$), subjected to uniform external pressure in the absence of elastic foundation, using both CST and TSDT approaches. The auxetic structure's geometric parameters are specified as follows: $\theta = 60°$, $r_c = 2$ mm, $d_1 = 2$ mm, $E_c = 69$ GPa. The analysis considers various *R/h* ratios and includes both convex (Table 2) and concave (Table 3) TSSs with two CNT distribution types: UD and FG-X. As observed, the discrepancy in the critical buckling loads between CST and TSDT is minimal for thin shells. However, for thicker shells, this difference becomes more pronounced. For instance, for convex TSSs (Table 2), at $R/h = 200$ (thin shell) with the FG-X CNT distribution, the critical load p_0^{cr} is 0.334489 MPa (CST) compared to 0.334214 MPa (TSDT), yielding a discrepancy of 0.08%. In contrast, at $R/h = 10$ (thick shell), the discrepancy increases to 3.55%. Similarly, for concave TSSs, the difference is 0.02% at $R/h = 200$, rising to 1.34% at $R/h = 8$. The table further shows that the discrepancy is higher for the FG-X distribution compared to UD, as expected, and is more significant for concave shells than for convex shells.

5.3 *Buckling analysis*

Tables 4-5 illustrate the impact of varying porosity coefficient (e_0) on the critical buckling load of arc-type auxetic core sandwich convex and concave porous TSSs under radial pressure. for convex TSSs ($a = 4R$), when $e_0 = 0$, the buckling load is 2.216 MPa. This load decreases by 1.40% at $e_0 = 0.2$, 2.87% at $e_0 = 0.4$, 4.47% at $e_0 = 0.6$, and 6.28% at $e_0 = 0.8$. A similar trend is observed for concave TSSs ($a = -3R$) with the same material and geometrical parameters, showing a 3.13% reduction in the critical buckling load as porosity increases. These findings highlight the detrimental effect of increased porosity on structural stability, as higher porosity coefficients compromise the critical buckling load for both convex and concave TSSs. This reduction is primarily attributed to the decreased effective stiffness of the porous face sheets; the presence of voids weakens the material's load-bearing capacity, diminishing the overall buckling

Table 4 Critical buckling load results for concave TSSs based on CST and TSDT approaches with arc-type auxetic core and CNTRC face sheets, subjected to uniform external pressure, across various R/h ratios. ($e_0 = 0, a = -4R, L = 1.5R, h_1 = 0.001$ mm, $\bar{V}_{CNT} = 0.17, K_1 = K_2 = 0$)

R/h	TSDT		CST		Difference (%)	
	UD	FG-X	UD	FG-X	UD	FG-X
8	162.164 (1,3)	178.743 (1,2)	163.945 (1,2)	181.14 (1,2)	1.10	1.34
20	14.9114 (1,3)	17.2868 (1,3)	15.0545 (1,3)	17.4702 (1,3)	0.96	1.06
50	1.5553 (1,4)	1.827 (1,4)	1.5607 (1,4)	1.83381 (1,4)	0.35	0.37
100	0.198078 (1,4)	0.232178 (1,4)	0.198247 (1,4)	0.232392 (1,4)	0.09	0.09
200	0.0263553 (1,4)	0.0306249 (1,4)	0.0263606 (1,4)	0.0306316 (1,4)	0.02	0.02

Table 5 Influence of porosity coefficients on the critical buckling loads of sandwich-structured convex TSSs with arc-type auxetic core and porous CNTRC face sheets, subjected to uniform external pressure and surrounded by a Kerr foundation (a=4R, R/h=80, L=1.5R, $h_1 = 1$ mm, $h_2 = 2$ mm, UD porosity distribution, $\theta = 45°$, $r_c = d_1 = 2$ mm, $K_l = K_u = 10^7$, $K_s = 10^5$, $\bar{V}_{CNT} = 0.17$, UD-CNT, y-direction)

Porosity coefficient	Critical Buckling Load (MPa)	Reduction in Buckling Load (%)
$e_0 = 0$	2.216 (2,6)	0.00
$e_0 = 0.2$	2.18501 (2,6)	1.40
$e_0 = 0.4$	2.15233 (2,6)	2.87
$e_0 = 0.6$	2.11702 (2,6)	4.47
$e_0 = 0.8$	2.07673 (2,6)	6.28

Table 6 Influence of porosity coefficients on the critical buckling loads of sandwich-structured concave TSSs with arc-type auxetic core and porous CNTRC face sheets, subjected to uniform external pressure and surrounded by a Kerr foundation (a=-3R, R/h=80, L=1.5R, $h_1 = 1$ mm, $h_2 = 2$ mm, UD porosity distribution, $\theta = 45°$, $r_c = d_1 = 2$ mm, $K_l = K_u = 10^7$, $K_s = 10^5$, $\bar{V}_{CNT} = 0.17$, UD-CNT, y-direction)

Porosity coefficient	Critical Buckling Load (MPa)	Reduction in Buckling Load (%)
$e_0 = 0$	0.830979 (1,3)	0.00
$e_0 = 0.2$	0.825184 (1,3)	0.70
$e_0 = 0.4$	0.819073 (1,3)	1.43
$e_0 = 0.6$	0.812475 (1,3)	2.23
$e_0 = 0.8$	0.804947 (1,3)	3.13

resistance of the shells. Table 7-8 compares the effect of various porosity distribution types on the critical buckling load of arc-type auxetic-core TSSs with porous face sheets under uniform radial pressure across varying porosity coefficients (e_0) ranging from 0 to 0.8. Among the three distribution types—uniform, symmetric, and asymmetric—the symmetric distribution consistently yields slightly lower critical buckling load values than the other two, regardless of the porosity coefficient. The highest buckling load values are observed for the asymmetric distribution. For example, in convex TSSs with $e_0 = 0.8$, the reduction in buckling load compared to no porosity is 6.28% for the uniform distribution, 5.50% for the symmetric distribution, and 5.35% for the asymmetric distribution. Similarly, in concave shells, the reductions are 3.13%, 2.74%, and 2.64%, respectively, demonstrating the same trend.

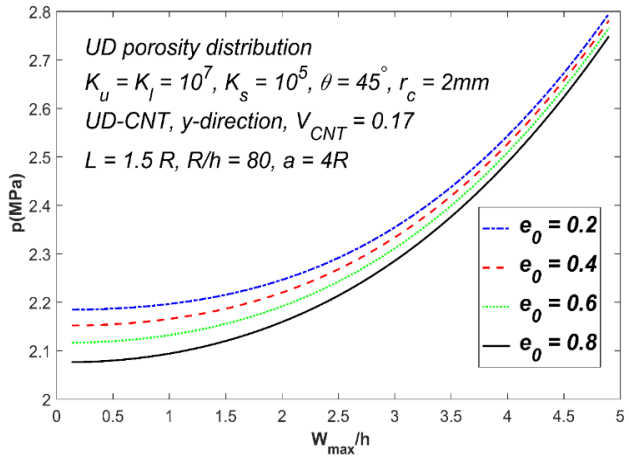

Fig. 3 Impact of porosity coefficient on the postbuckling curves of convex TSSs

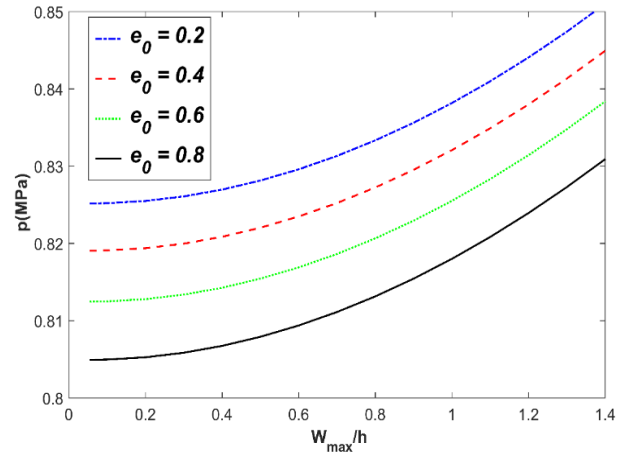

Fig. 4 Impact of porosity coefficient on the postbuckling curves of concave shells (UD porosity distribution, a=-3R, R/h=80, L=1.5R, $h_1 = 1$ mm, $h_2 = 2$ mm, $\theta = 45°$, $r_c = d_1 = 2$ mm, $K_l = K_u = 10^7$,$K_s = 10^5$, $\bar{V}_{CNT} = 0.17$, UD-CNT, y-direction)

5.4 Postbuckling analysis

Figs. 3-4 illustrate the influence of varying porosity coefficients on the postbuckling response of porous sandwich composite convex and concave TSSs, plotted against normalized deflections ($W_{\max}/h$). It is observed that increasing e_0 consistently reduces the postbuckling equilibrium path, indicating the detrimental influence of porosity on the load-bearing capability of the shells. At $e_0 = 0.2$, the structure demonstrates the highest postbuckling strength, maintaining superior stability throughout the deformation process. However, as e_0 increases, progressive degradation in stiffness occurs, significantly limiting the shell's resistance to external loads.

Figs. 4-5 show the postbuckling curves of porous convex sandwich TSSs, illustrating the effect of various porosity patterns on critical buckling loads. While the postbuckling curve trends are similar across all three porosity distribution types, uniform porosity results in the lowest critical

buckling load among the three distribution types. The postbuckling curve for TSSs with asymmetric porosity is marginally more significant than that for UD porosity distribution.

6. Conclusions

This paper investigates the effects of porosity in the nonlinear buckling and postbuckling characteristics of shear-deformable arc-type auxetic-core sandwich TSSs with porous CNT-reinforced face sheets surrounded by a Kerr-type foundation and subjected to external pressure. Fundamental equations are derived using the Airy stress function and TSDT, incorporating von Kármán-type geometric nonlinearity, with the Galerkin procedure employed to determine explicit load-deflection relationships. The numerical findings yield several key insights:

- For thin TSSs, the difference between critical buckling loads obtained from CST and TSDT is minimal, validating the applicability of CST for these cases. Therefore, CST is sufficient to study the stability of thin shells. However, for thicker shells, where discrepancies up to 3.55% are observed—particularly with FG-X CNT distribution and concave shapes—TSDT provides a more accurate stability analysis, demonstrating its necessity for thicker TSSs.
- Increasing porosity decreases the stability of porous sandwich TSSs. For example, the buckling load of convex TSSs decreases by up to 6.28%, while concave TSSs exhibit a reduction of 3.13%. Higher porosity also reduces postbuckling strength.
- Among the three porosity distribution types, the UD type has the most adverse impact, resulting in the lowest critical buckling loads and the weakest postbuckling performance.
- Given the significant role of porosity in reducing the stiffness of sandwich shells, a realistic and thorough analysis of the stability of sandwich TSSs requires an accurate assessment of the porosity coefficient and its distribution.

References

Ashby, M.F. and Gibson, L.J. (1997), *Cellular Solids: Structure and Properties*, Press Syndicate of the University of Cambridge, Cambridge, UK.

Duc, N.D., Kim, S.E., Quan, T.Q., Manh, D.T. and Cuong, N.H. (2020), "Nonlinear buckling of eccentrically stiffened nanocomposite cylindrical panels in thermal environments", *Thin Wall. Struct.*, **146**, 106428. https://doi.org/10.1016/j.tws.2019.106428.

Dung, D.V. and Vuong, P.M. (2017), "Analytical investigation on buckling and postbuckling of FGM toroidal shell segment surrounded by elastic foundation in thermal environment and under external pressure using TSDT", *Acta Mechanica*, **228**(10), 3511-3531. https://doi.org/10.1007/s00707-017-1888-2

Ebrahimi, F. (2024), *Mechanics of Auxetic Materials and Structures*, CRC Press.

Ebrahimi, F. and Ahari, M.F. (2024), "On the buckling of meta-graphene-origami-enabled magnetostrictive nanoplates under temperature gradient", *Acta Mechanica*, **235**(5), 2611-2628. https://doi.org/10.1007/s00707-024-03861-x.

Ebrahimi, F. and Dabbagh, A. (2020), *Mechanics of Nanocomposites: Homogenization and Analysis*, CRC Press.

Ebrahimi, F. and Dabbagh, A. (2023), "Porosity effects on static performance of carbon nanotube-reinforced meta-nanocomposite structures", *Micromach.*, **14**(7), 1402. https://doi.org/10.3390/mi14071402.

Ebrahimi, F. and Dadashi, M. (2023), "Composite cylindrical shells with auxetic core on elastic foundation: A nonlinear dynamic analysis", *Struct.*, **57**, 105170. https://doi.org/10.1016/j.istruc.2023.105170.

Ebrahimi, F. and Seyfi, A. (2022), "Studying propagation of wave of metal foam rectangular plates with graded porosities resting on Kerr substrate in thermal environment via analytical method", *Wave. Random Complex Media*, **32**(2), 832-855. https://doi.org/10.1080/17455030.2020.1802531.

Ebrahimi, F., Dabbagh, A. and Rastgoo, A. (2019), "Vibration analysis of porous metal foam shells rested on an elastic substrate", *J. Strain Anal. Eng. Des.*, **54**(3), 199-208. http://doi.org/10.1177/0309324719852555.

Ebrahimi, F., Goudarzfallahi, M. and Ziazi, A.A. (2024a), "Static stability analysis of graphene origami-reinforced nanocomposite toroidal shells with various auxetic cores", *Adv. Nano Res.*, **17**(1), 1. https://doi.org/10.12989/anr.2024.17.1.001.

Ebrahimi, F., Goudarzfallahi, M. and Ziazi, A.A. (2024b), "Buckling and post-buckling analysis of sandwich toroidal shell composites with graphene origami-enabled auxetic metamaterial core under combined mechanical loads", *Compos.: Mech. Comput. Appl.*, https://doi.org/10.1615/CompMechComputApplIntJ.2024054751.

Ebrahimi, F., Goudarzfallahi, M. and Ziazi, A.A. (2024c), "Porosity effects on the buckling and post buckling of metamaterial sandwich toroidal shell segments", *Steel Compos. Struct.*, **53**(3), 313-326. https://doi.org/10.12989/scs.2024.53.3.313.

Ebrahimi, F., Goudarzfallahi, M. and Ziazi, A.A. (2024d), "Nonlinear stability analysis of shear-deformable sandwich meta-composite shell with arc-type auxetic core.", *Adv. Nano Res.*, **17**(6), 547. https://doi.org/10.12989/anr.2024.17.6.547

Ebrahimi, F., Goudarzfallahi, M. and Ziazi, A.A. (2025a), "Buckling and postbuckling analysis of graphene origami-enabled auxetic metamaterial sandwich toroidal shell segments subjected to axial compression", *J. Eng. Mech.*, **151**(5), 04025012. https://doi.org/10.1061/jenmdt.emeng-7954.

Ebrahimi, F., Goudarzfallahi, M. and Ziazi, A.A. (2025b), "Enhancing nonlinear static stability behavior of axially compressed sandwich composite toroidal shells with a bio-inspired auxetic core", *Acta Mechanica*, 1-18.

Fu, T., Wang, X., Hu, X. and Rabczuk, T. (2024), "Impact dynamic response of stiffened porous functionally graded materials sandwich doubly-curved shells with Arc-type auxetic core", *Int. J. Impact Eng.*, **191**, 105000. https://doi.org/10.1016/j.ijimpeng.2024.105000.

Hieu, P.T. and Van Tung, H. (2020a), "Buckling of shear deformable FG-CNTRC cylindrical shells and toroidal shell segments under mechanical loads in thermal environments", *ZAMM-J. Appl. Math. Mech./Zeitschrift für Angewandte Mathematik und Mechanik*, **100**(11), e201900243. https://doi.org/10.1177/0892705719853611.

Hieu, P.T. and Van Tung, H. (2020b), "Thermal and thermomechanical buckling of shear deformable FG-CNTRC cylindrical shells and toroidal shell segments with tangentially restrained edges", *Arch. Appl. Mech.*, **90**(7), 1529-1546. https://doi.org/10.1007/s00419-020-01682-7.

Hieu, P.T. and Van Tung, H. (2021), "Thermal buckling and postbuckling of CNT-reinforced composite cylindrical shell surrounded by an elastic medium with tangentially restrained edges", *J. Thermoplast. Compos. Mater.*, **34**(7), 861-883. https://doi.org/10.1177/0892705719853611.

Hoai Nam, V., Ngoc Ly, L., Thi Kieu My, D., Minh Duc, V. and Thi Phuong, N. (2024), "On the nonlinear buckling and postbuckling responses of sandwich FG-GRC toroidal shell segments with corrugated core under axial tension and compression in the thermal environment", *Polym. Compos.*, **45**(15), 13737-13752. https://doi.org/10.1002/pc.28732.

Li, Y.S. and Liu, B.L. (2022), "Thermal buckling and free vibration of viscoelastic functionally graded sandwich shells with tunable auxetic honeycomb core", *Appl. Math. Model.*, **108**, 685-700. https://doi.org/10.1016/j.apm.2022.04.019.

Nam, V.H., Duc, V.M., Doan, C.V., Thanh Xuan, N.T. and Phuong, N.T. (2022), "Nonlinear postbuckling behavior of auxetic-core toroidal shell segments with Graphene reinforced face sheets under axial loads", *Arch. Mech.*, **74**(2-3), 89-108. http://doi.org/10.24423/aom.3957.

Nam, V.H., Phuong, N.T. and Duc, V.M. (2019), "Nonlinear buckling of orthogonal carbon nanotube-reinforced composite cylindrical shells under axial compression surrounded by elastic foundation in thermal environment", *Int. J. Comput. Mater. Sci. Eng.*, **8**(04), 1950016.

https://doi.org/10.1142/S2047684119500167.
Nguyen, T.P., Vu, M.D., Dang, T.D., Cao, V.D., Pham, T.H. and Vu, H.N. (2023), "An analytical approach of nonlinear buckling behavior of torsionally loaded auxetic core toroidal shell segments with graphene reinforced polymer coatings", *Adv. Compos. Mater.*, **32**(3), 400-418. https://doi.org/10.1080/09243046.2022.2110661.
Oyesanya, M.O. (2005), "Influence of extra terms on asymptotic analysis of imperfection sensitivity of toroidal shell segment with random imperfection", *Mech. Res. Commun.*, **32**(4), 444-453. https://doi.org/10.1016/j.mechrescom.2005.02.006.
Phuong, N.T., Nam, V.H., Trung, N.T., Duc, V.M., Van Loi, N., Thinh, N.D. and Tu, P.T. (2021), "Thermomechanical postbuckling of functionally graded graphene-reinforced composite laminated toroidal shell segments surrounded by Pasternak's elastic foundation", *J. Thermoplast. Compos. Mater.*, **34**(10), 1380-1407. https://doi.org/10.1177/0892705719870593.
Phuong, N.T., Van Doan, C., Duc, V.M., Giang, N.T. and Nam, V.H. (2023), "Analytical solution for nonlinear buckling of convex and concave auxetic-core toroidal shell segments with graphene-reinforced face sheets subjected to radial loads", *Arch. Appl. Mech.*, **93**(2), 621-634. https://doi.org/10.1007/s00419-022-02288-x.
Reddy, J.N. (2003), *Mechanics of Laminated Composite Plates and Shells: Theory and Analysis*, CRC Press.
Reddy, J.N. and Liu, C.F. (1987), "A higher-order theory for geometrically nonlinear analysis of composite laminates", No. VPI-E-86.21, NASA.
Shen, H.S. (2011a), "Postbuckling of nanotube-reinforced composite cylindrical shells in thermal environments, Part I: Axially-loaded shells", *Compos. Struct.*, **93**(8), 2096-2108. https://doi.org/10.1016/j.compstruct.2011.02.011.
Shen, H.S. (2011b), "Postbuckling of nanotube-reinforced composite cylindrical shells in thermal environments, Part II: Pressure-loaded shells", *Compos. Struct.*, **93**(10), 2496-2503. https://doi.org/10.1016/j.compstruct.2011.04.005.
Shen, H.S. and Xiang, Y. (2013), "Postbuckling of nanotube-reinforced composite cylindrical shells under combined axial and radial mechanical loads in thermal environment", *Compos. Part B: Eng.*, **52**, 311-322. https://doi.org/10.1016/j.compositesb.2013.04.034.
Stein, M. and McElman, J.A. (1965), "Buckling of segments of toroidal shells", *AIAA J.*, **3**(9), 1704-1709. https://doi.org/10.2514/3.55185.
Van Quyen, N., Van Thanh, N., Quan, T.Q. and Duc, N.D. (2021), "Nonlinear forced vibration of sandwich cylindrical panel with negative Poisson's ratio auxetic honeycombs core and CNTRC face sheets", *Thin Wall. Struct.*, **162**, 107571. https://doi.org/10.1016/j.tws.2021.107571.
Van Tien, N., Duc, V.M., Nam, V.H., Phuong, N.T., Ho, L.S., Dong, D.T., ... & Minh, T.Q. (2022), "Nonlinear postbuckling of auxetic-core sandwich toroidal shell segments with CNT-reinforced face sheets under external pressure", *Int. J. Struct. Stab. Dyn.*, **22**(01), 2250006. https://doi.org/10.1142/S0219455422500067.
Vuong, P.M. and Duc, N.D. (2019), "Nonlinear buckling and postbuckling of a FGM toroidal shell segment under a torsional load in a thermal environment within Reddy's third-order shear deformation shell theory", *Mech. Compos. Mater.*, **55**, 467-482. https://doi.org/10.1007/s11029-019-09826-9.
Vuong, P.M. and Duc, N.D. (2020a), "Nonlinear static and dynamic stability of functionally graded toroidal shell segments under axial compression", *Thin Wall. Struct.*, **155**, 106973. https://doi.org/10.1016/j.tws.2020.106973.
Vuong, P.M. and Duc, N.D. (2020b), "Nonlinear buckling and post-buckling behavior of shear deformable sandwich toroidal shell segments with functionally graded core subjected to axial compression and thermal loads", *Aerosp. Sci. Technol.*, **106**, 106084. https://doi.org/10.1016/j.ast.2020.106084.
Wang, X. and Fu, T. (2024), "A novel arc-type auxetic cellular doubly-curved shells with negative Poisson's ratio for broadband low-frequency sound insulation", *Eur. J. Mech.-A/Solid.*, **106**, 105326. https://doi.org/10.1016/j.euromechsol.2024.105326.
Zhao, L.C., Xu, L. and Zeng, H.T. (2024), "Thermal buckling of temperature-dependent FG-CNT reinforced composite conical-conical joined shell using GDQ", *Thin Wall. Struct.*, **205**, 112320.

https://doi.org/10.1016/j.tws.2024.112320.

AP